Nanoscale

ROYAL SOCIETY OF CHEMISTRY

PAPER

View Article Online
View Journal | View Issue

Cite this: *Nanoscale*, 2025, **17**, 22484

Microwave-assisted growth of Ag nanoparticles on Ti_3CNT_x MXene for antibacterial food packaging

Madhurya Chandel, *[a] Michał Jakubczak, [a,b]
Muhammad Abiyyu Kenichi Purbayanto, [a,b] Agnieszka Górnik,[b] Weronika Basior,[b]
Dorota Moszczyńska,[b] Anika Tabassum, [c,d] Michael Naguib [c,d] and
Agnieszka Maria Jastrzębska *[a]

MXenes, particularly titanium-based carbides, have been extensively studied, while other compositions remain relatively unexplored. Ti_3CNT_x (carbonitrides) exhibit unique catalytic, optical, and electronic properties, yet their bioactivity is under-investigated. This study utilizes a microwave-assisted method to selectively etch aluminum from the Ti_3AlCN MAX phase, producing multi-layered (ML) Ti_3CNT_x. *In situ* silver (Ag) nanoparticles are grown on these layers, forming Ag/Ti_3CNT_x MXene nanocomposites. Unlike conventional approaches using prolonged 48% HF treatments (24 h), this work employs a more efficient, safer, and time-effective method with 6 M HCl for just 4 hours. The antimicrobial potential of ML Ti_3CNT_x and Ag/Ti_3CNT_x is evaluated against Gram-positive and Gram-negative bacteria (*Escherichia coli*, *Staphylococcus aureus*, and *Bacillus subtilis*) *via* bacterial growth curve analysis, revealing a 20% enhancement in antibacterial efficacy with Ag/Ti_3CNT_x. When incorporated into food packaging materials such as paper, these nanocomposites exhibit strong potential for biomedical and food safety applications. However, thorough market analyses and material safety evaluations are essential before commercial deployment.

Received 19th May 2025,
Accepted 25th August 2025

DOI: 10.1039/d5nr02098k

rsc.li/nanoscale

1 Introduction

Packaging is essential for maintaining food quality from production to consumption by overcoming various challenges.[1,2] The global population increase has heightened food demand, and urbanization has made consumers seek high-quality, safe, and easily accessible food. Various preservation methods, such as wax coating, plastic packaging films, and refrigeration, have positive and negative impacts.[2,3] For instance, wax coatings are difficult to clean, affecting taste and potentially causing health issues due to reduced gas exchange and limited biodegradability. Plastic packaging lacks antibacterial and antioxidant properties, leading to inadequate preservation. It is non-degradable and harms ecosystems at an alarming rate.[2–4] Therefore, developing environmental friendly, simple, and efficient preservation materials with multiple protective functions for advanced food preservation is urgent.

Nanomaterials have recently emerged as excellent antibacterial agents and food packaging materials. They have a higher chance of overcoming bacterial resistance than antibiotics due to their superior membrane permeability and biocompatibility.[1,2,5] Nanomaterial-based food packaging offers many benefits over traditional methods, such as improved temperature resistance, durability, flame resistance, and material delivery in biological systems, cost-effectively and sustainably.[2,4–7] Various 2D nanomaterials, including graphene and MXene, have been used for antibacterial and other biomedical applications.[8–12]

MXenes are two-dimensional (2D) materials of transition metal carbide, nitride, or carbonitride. They are generally represented by the formula $M_{n+1}X_nT_x$, where M is an early transition metal, X is either nitrogen or carbon, n ranges from 1 to 4, and T_x denotes surface functional groups (–O, –OH, –F, –Cl). MXenes have shown some antimicrobial performance in specific conditions, yet it has to be fully explored.[13,14] A significant advantage of MXenes over other nanomaterials lies in the tunability of their atomic structure, composition, and surface terminations, which is an exciting opportunity to adjust their antimicrobial activities. MXenes may confer antibacterial effects through various physical and chemical mechanisms

---

[a] Warsaw University of Technology, Faculty of Mechatronics, św. Andrzeja Boboli 8, 02-525 Warsaw, Poland. E-mail: madhurya.chandel@pw.edu.pl, agnieszka.jastrzebska@pw.edu.pl

[b] Warsaw University of Technology, Faculty of Materials Science and Engineering, Wołoska 141, 02-507, Poland

[c] Department of Physics and Engineering Physics, Tulane University, New Orleans, LA 70118, USA

[d] Department of Chemistry, Tulane University, New Orleans, LA 70118, USA

(including direct physical contact, oxidative stress, photothermal ablation, photocatalytic activity, and multi-mode synergistic antibacterial effects). Therefore, they can be used in drug delivery, photodynamic therapy, food-packaging industries, and other medical applications.[3,12,14,15]

MXenes have shown some antibacterial potential and low toxicity towards human cells.[11,16–19] Specifically, the first reported MXene, $Ti_3C_2T_x$, showed high antibacterial properties against *Escherichia coli (E. coli)* and *Bacillus subtilis (B. subtilis)*.[14] The $Ti_3C_2T_x$ MXene acts *via* physical mechanisms, including contact-mediated adhesion, which disrupts cell wall and cell membrane integrity and leads to the leaking of intracellular contents.[14] Wrapping of MXene sheets around bacterial cells also occurs with the application of increased concentration of MXenes and chemical mechanisms induced by $Ti_3C_2T_x$.[10,11] The $Ti_3C_2T_x$ MXene induced reactions with some components of the cell wall and cell membrane, compromising their morphology.[10,14,15]

In the MXene family, around 100 MXenes have been predicted theoretically, and more than 50 MXenes have been reported experimentally.[20,21] Although approximately 70% of MXene research focuses on $Ti_3C_2T_x$, it is equally crucial to explore other MXenes.[10] Ti_3CNT_x MXene, discovered in 2012,[22] has since found widespread applications in energy storage devices (such as batteries and supercapacitors), self-cleaning surfaces (*e.g.*, organic dyes), photonic applications, catalysis, and electromagnetic interference shielding.[23–30] Its behavior stands out compared to its carbide counterparts, making it an essential member of the carbonitride MXene family due to its intriguing physical and chemical properties.[25,31] Therefore, it is equally important to pay attention and explore other MXenes. Like other MXenes, Ti_3CNT_x hydrophilicity makes it a potential candidate for many biomedical and food packaging applications due to the high water content of biological systems and food items (such as fruits and vegetable dairy products).[3,11,12,21,26,31,32] To our knowledge, this study is the first to report on the antibacterial properties of Ti_3CNT_x, Ag/Ti_3CNT_x, and their potential use in food packaging applications.

Ag nanoparticles combined with $Ti_3C_2T_x$ have shown improved antibacterial performance compared to $Ti_3C_2T_x$ alone.[33,34] However, these studies relied on either light activation or high silver content (over 20%), and the material synthesis took over 30–40 hours, making the process challenging. Other transition metal nanoparticles, especially noble metals like Pt, Ru, and Au, have also been used in similar nanocomposites with good results,[35–37] but their high cost makes them less viable than silver.[38,39]

In this study, we present a novel approach involving the *in situ* growth of silver nanoparticles (10 wt%) on etched multilayer (ML) Ti_3CNT_x MXene to create MXene-based nanocomposites, denoted as silver-MXene (Ag/Ti_3CNT_x). The nanocomposites were synthesized using a microwave-assisted hydrothermal method, completing the reaction in just 6 hours, including MAX phase etching. This approach sets the work apart from previously reported MXene and MXene-based materials.[9,14,33,37] Further, our investigation focused on the antibacterial activity of these nanocomposites against three different bacterial strains: *E. coli*, *S. aureus*, and *B. subtilis*. By combining ML Ti_3CNT_x MXene with Ag nanoparticles, we aimed to gain a deeper understanding of their roles.

Incorporating 10 wt% silver (Ag) into MXene enabled us to explore its tunable antibacterial and cytotoxic properties. Incorporation of 10 wt% Ag was decided on the basis of literature and previous research work.[33,40,41] Silver nanoparticles are known to be effective antimicrobial agents in packaging films, helping prevent microbial growth on food contact surfaces.[33,34] We further evaluated antibacterial activity using real samples such as packaging paper, bread, and cheese, as detailed in the Experimental section. Overall, this study, from MAX phase etching to the synthesis of Ag/Ti_3CNT_x nanocomposites and their antibacterial testing, presents a novel and unique approach for food packaging applications.

2 Materials and methods

2.1 Chemicals and reagents used

Hydrochloric acid (HCl) with 37% (v/v) concentration, HNO_3 from Merck (Darmstadt, Germany), PVP (Polyvinylpyrrolidone), $AgNO_3$ (0.1 N) solution, LiF (Lithium fluoride), and EG (ethylene glycol) were purchased from Chempur (Piekary Śląskie, Poland). Double distilled water was used. Mueller–Hinton broth and 2.5% glutaraldehyde solution (Sigma-Aldrich, Saint Louis, MO, USA), phosphate-buffered saline (PBS, Carl Roth, Karlsruhe, Germany), *Escherichia coli* (*E. coli*, ATCC 10799), *Staphylococcus aureus* (*S. aureus*, ATCC 29213), and *Bacillus subtilis* (*B. subtilis*, ATCC 11774) bacterial strains were used in microbiological studies. All the chemicals were used without further purification.

2.2 Synthesis of Ti_3CNT_x MXene using microwave-assisted hydrothermal method

Initially, 400 mg of LiF was slowly added to 6 M HCl and stirred for 10 min. After that, 1 g of MAX phase (Ti_3AlCN) powder was added slowly and stirred for 10 min. Then, the reaction mixture was transferred into a teflon container and heated in a microwave reactor for 4 hours at 150 °C. Then, the precipitate was washed with distilled water using centrifuges at 6000 rpm for 4 min each until pH reached 6. Further, it was used to prepare Ag/Ti_3CNT_x and characterization.

2.3 Synthesis of silver nanoparticles using microwave-assisted hydrothermal method

Initially, 15 mg of fresh AgCl was prepared from 15 ml of 0.1 N $AgNO_3$ solution using 0.5 ml of HNO_3 (6 M) and 5 ml of HCl (6 M) in a 10 ml beaker. Fresh AgCl precipitates were washed with distilled water first and later with acetone. Further, it was kept for drying in a 10 ml beaker in the open-air atmosphere at room temperature (~25 °C). The fresh AgCl precipitate will work as a seed to grow different morphologies of Ag nanoparticles.

Further, the $AgNO_3$ solution was added dropwise to 10 ml of ethylene glycol (EG) and stirred continuously. In another 50 ml beaker, 100 mg of polyvinylpyrrolidone (PVP) was dissolved in 10 ml of EG until the solution became clear. Fresh AgCl precipitates were added to the PVP solution in EG and stirred until the solution cleared again. Subsequently, the PVP with EG and AgCl solution was added dropwise into EG with $AgNO_3$ solution under constant stirring. Next, the final reaction mixture was transferred into a teflon container and heated for 150 minutes at 165 °C. The white-grey precipitate was formed, washed with acetone, and left to dry at room temperature (~25 °C) in an open-air atmosphere.

2.4 Synthesis of Ag/Ti_3CNT_x nanocomposites

Initially, Ti_3CNT_x was prepared by etching out Al from Ti_3AlCN using a microwave-assisted hydrothermal method, as reported in our previous paper.[26] After that, Ag is grown *in situ* on this multilayer (ML) Ti_3CNT_x using a polyol-based microwave-assisted hydrothermal method. The same protocol (Section 2.3) has been followed with addition of ML-Ti_3CNT_x. Here, the fresh AgCl precipitate will work as a seed to grow Ag nanoparticles *in situ* on the surface of ML-Ti_3CNT_x.[42]

At the end of the process, 250 mg of ML Ti_3CNT_x MXene powder was added slowly, and the final reaction mixture was transferred into a Teflon container and heated for 150 minutes at 165 °C. Ultimately, blackish-light grey precipitates were formed, washed with acetone, and left to dry at room temperature (~25 °C). According to the reference, synthesis of MAX phases was carried out.[22,26]

2.5 Characterization

Ti_3AlCN, Ti_3CNT_x, and Ag/Ti_3CNT_x morphology were studied using scanning electron microscopy (SEM, Hitachi S3500N and Hitachi S5500, Tokyo, Japan). The samples for SEM imaging were prepared either on aluminum or copper substrates. Further size and interlayer spacing were calculated using ImageJ software. Energy-dispersive X-ray spectroscopy (EDS) was used to study the elemental composition of the samples. X-ray diffraction (XRD) patterns were measured to evaluate the purity and crystal structure of the samples using Bruker D8 Advanced, Billerica, MA.

The zeta potential was characterized using a Zetasizer (NANO ZS ZEN3500 analyzer, Malvern Instruments, Malvern, UK) equipped with a back-scattered light detector and operating at 173°. The results are an average of 10 repeated measurements. The surface functionalization and chemical composition were studied using Attenuated Total Reflectance-Fourier transform infrared (ATR-FTIR) spectroscopy (Nicolet iS5, Thermo Scientific, Waltham, MA).

Furthermore, the optical properties were studied by double-beam scanning UV-visible spectroscopy (Evolution 220, Thermo Scientific) equipped with an integrating sphere. For powder samples, solid sample holders were used with a quartz glass window, and the data were taken using a diffuse reflectance (DRS) mode at 400–1000 nm with a scanning speed of 200 nm min^{-1}.

2.6 Bacterial suspension preparation and antibacterial properties assay

Model bacteria strains were obtained from the American Type Culture Collection (ATCC). In this study, we used the *Escherichia coli* (*E. coli*, ATCC 10799), *Staphylococcus aureus* (*S. aureus*, ATCC 29213), and *Bacillus subtilis* (*B. subtilis*, ATCC 11774) bacterial strains. Directly before the studies, bacteria were cultivated on Tryptic Soy Agar (TSA, Merck, Darmstadt, Germany) solid medium in Petri dishes for 24 h at 37 ± 2 °C. Further, bacteria were collected and washed multiple times using phosphate-buffered saline (PBS, Carl Roth, Karlsruhe, Germany) and centrifugation (3000 rpm) to remove any residues of cultured macromolecules. In the last step, bacterial pellets were resuspended in the Mueller–Hinton broth (Sigma-Aldrich, Saint Louis, MO, USA) and used in further studies.

Antibacterial properties assay involved preparing a series of dilutions of the synthesized nanomaterials and further incubation in the presence of *E. coli*, *S. aureus*, and *B. subtilis* bacterial strains. The biocidal action was evaluated by measuring optical density at 610 nm (OD_{610}), which correlates with the number of bacterial cells, using a multi-plate reader Infinite 200 Pro (Tecan, Männedorf, Switzerland). The research was conducted in the Mueller–Hinton broth, commonly used in minimum inhibitory concentration (MIC) tests. The following dilutions were prepared to examine the effect of the presence of developed Ti_3CNT_x MXene and its modification with Ag on bacterial growth: 0 (control), 16, 32, 62.5, 125, 250, 375, and 500 mg L^{-1}. In the next step, bacterial suspensions were added to obtain the final concentration of approximately 10^8 CFU mg L^{-1} (McFarland standard no. 1). The batch assays were subjected to continuous shaking at 300 rpm and a constant temperature of 37 ± 2 °C. Measurements of OD_{610} have been performed every hour from 0 to 16 h and then after 24, 48, and 72 h.

Bacterial growth curves were created by plotting OD values *versus* time and studying bacterial growth kinetics. Next, the percent viability (V) of microorganisms' growth was assessed according to eqn (1):

$$V(\%) = \frac{N}{N_0} \times 100 \tag{1}$$

where V is the viability of bacteria, N is the OD610 measured during the incubation (t_n, where n stands for 8, 16, 24, 48, and 72 h), and N_0 is the OD_{610} measured at the beginning of the experiment (t_0). For the samples measured in t_0, we assumed 100% viability. All experiments were performed in triplicate, and the data were shown as mean ± standard deviation (SD).

After viability calculation using eqn (1), the data were analyzed for statistical significance using Microsoft Excel. Comparisons between two groups were made with Student's *t*-test. A p-value of less than 0.05 was considered statistically significant.

2.7 Bacterial sample preparation for SEM characterization

To elucidate the effect of developed materials on the morphology and surface structure of bacterial cells, we utilized SEM Hitachi S5500N. Samples for SEM were prepared as follows. First, cells after the experiments were fixed with 2.5% glutaraldehyde solution at 4 °C overnight. This was followed by multiple washings with PBS and dehydration, gradually increasing ethanol concentrations (12.5, 25, 50, 75, 100%). Before SEM observations, ethanol was exchanged with isopropyl alcohol, and samples were transferred onto the surface of the copper grid with carbon mesh. After isopropanol had evaporated completely, samples were studied with SEM using an accelerating voltage of 15.0 kV without additional conductive coating due to sufficient conductivity.

2.8 Antibacterials studies of actual samples for food packaging applications

For our antibacterial studies on food packaging applications, we used three real-world samples: (i) laboratory-grade tissue paper, (ii) Polish white (whole wheat) bread (Putka, Jawczyce, Poland), and (iii) cheddar cheese (Hochland Polska, Kazimierz, Poland), each cut into 4–8 cm^2 pieces. These samples were placed in Petri dishes and labeled. Each sample was divided into four sections: (i) blank, (ii) Ag (silver) nanoparticles, (iii) ML Ti_3CNT_x, and (iv) Ag/Ti_3CNT_x. All samples were sterilized under UV light for 1 hour before applying any bacterial solution.

We tested these sections against three bacterial strains: *E. coli*, *S. aureus*, *and B. subtilis*. Each bacterial strain solution was sprayed onto all samples, followed by the synthesized nanomaterials. The samples were incubated in two environments: (i) at 37 ± 2 °C and (ii) at room temperature (October temperature in Poland, 22 ± 2 °C). Images were captured continuously over 8 days.

After incubation, the bread and cheese samples were added to PBS solution, drop-cast onto glass slides, and imaged using an optical microscope (OPTA-TECH MB 200, Warsaw, Poland) with in-built *Capture 3.0 software* at different resolutions to observe bacterial growth. For the tissue paper, a small part was cut with a sterilized pair of scissors, placed on a glass slide, and imaged. All results are discussed in detail in the next section.

3 Results

3.1. Physical characterization

Given the increasing number of novel MXenes being reported, developing synthesis approaches that are chemically safe, easy to implement, and less time-consuming becomes challenging.[20] The microwave-assisted hydrothermal method addresses these challenges effectively. This technique allows precise control over the final product's size, shape, distribution, and crystallinity while avoiding oxidation by adjusting process parameters. Moreover, it produces a uniform and homogeneous product, crucial for consistent results.[43,44]

Microwave heating offers significant advantages, including minimizing heat loss and reducing the reaction time from several hours, as traditional wet-chemical synthesis requires, to just a few minutes.[43–45] This efficiency is difficult to achieve with other synthesis methods. Therefore, considering these benefits, we synthesized Ag/Ti_3CNT_x using a microwave-assisted hydrothermal method combined with a polyol process. The synthesis process is represented in Fig. 1.

Here, we have etched out Al from Ti_3AlCN MAX (Fig. 2a) phase *via* the microwave-assisted hydrothermal method to subsequent conversion into multilayer (ML) Ti_3CNT_x MXene (Fig. 2b). A detailed description of the procedure was reported in our previous paper.[26] From SEM images, a multilayer accordion-like Ti_3CNT_x (Fig. 2b) structure is visible, which confirms the successful etching of Al from the MAX phase. Further, we have grown Ag nanoparticles *in situ* on the surface of ML Ti_3CNT_x using the polyol method and prepared Ag/Ti_3CNT_x nanocomposites, shown in Fig. 2c. It also depicts that the *in situ* growth of Ag gives better binding with the ML Ti_3CNT_x MXene surface compared to physical mixing and makes it an interesting nanocomposite for further study.[24] The interlayer spacing (void between accordion structure) of Ti_3CNT_x MXene after etching, measured using ImageJ, ranged from 500 nm to 3 μm, confirming successful etching. Silver nanoparticles were characterized both with and without MXene. Without MXene, they formed various shapes, nanorods (0.5–2 μm long), cubes, and spheres, with particle sizes between 100 and 500 nm, likely due to the polyol method and PVP surfactant.[42,46] In contrast, Ag/Ti_3CNT_x composites mainly showed spherical and some distorted nanoparticles, sized between 50 and 400 nm, with interlayer spacing (void between accordion structure) ranging from 300 nm to 2 μm.

We have also prepared Ag nanoparticles without MXene using the same microwave-assisted polyol method shown in Fig. 2d. SEM images show different morphologies, from spherical nanoparticles to nanocubes and nanorods, making them unique to study. These results confirm that the *in situ* growth synthesis is more helpful and strongly binds with MXene nanocomposites. Further analysis using energy dispersive spectroscopy (EDS) mapping was used to identify the elemental composition of the materials. Elemental color mapping of Ti_3AlCN (Fig. S1 and Table S1) and Ti_3CNT_x (Fig. S2 and Table S2) confirm the etching of Al in the ML Ti_3CNT_x MXene. In the case of Ag/Ti_3CNT_x (Fig. 2e) and (Table S3), the uniform growth and confirmation of 10 wt% Ag is verified along with oxygen, which is associated with the surface functionalization of MXene. We have further used FT-IR measurement to cross-verify this claim, shown in Fig. S3. It shows the presence of hydroxyl and another oxygen-based functional group in the spectra. It is visible and strong in the case of Ag/Ti_3CNT_x nanocomposites compared to ML Ti_3CNT_x. Also, for Ti_3AlCN, we did not observe any peak compared to ML Ti_3CNT_x and Ag/Ti_3CNT_x nanocomposites.

Furthermore, XRD measurements were performed to understand the purity and correct phase formation. The diffraction peaks (mainly (014) peak) of parent MAX phase Ti_3AlCN

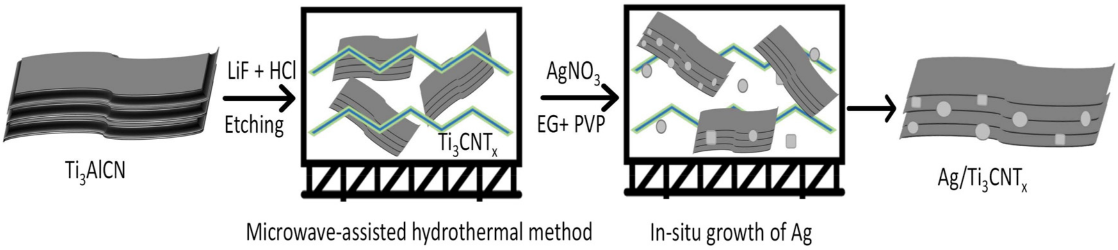

Fig. 1 A graphical representation of the synthesis of Ag/Ti_3CNT_x.

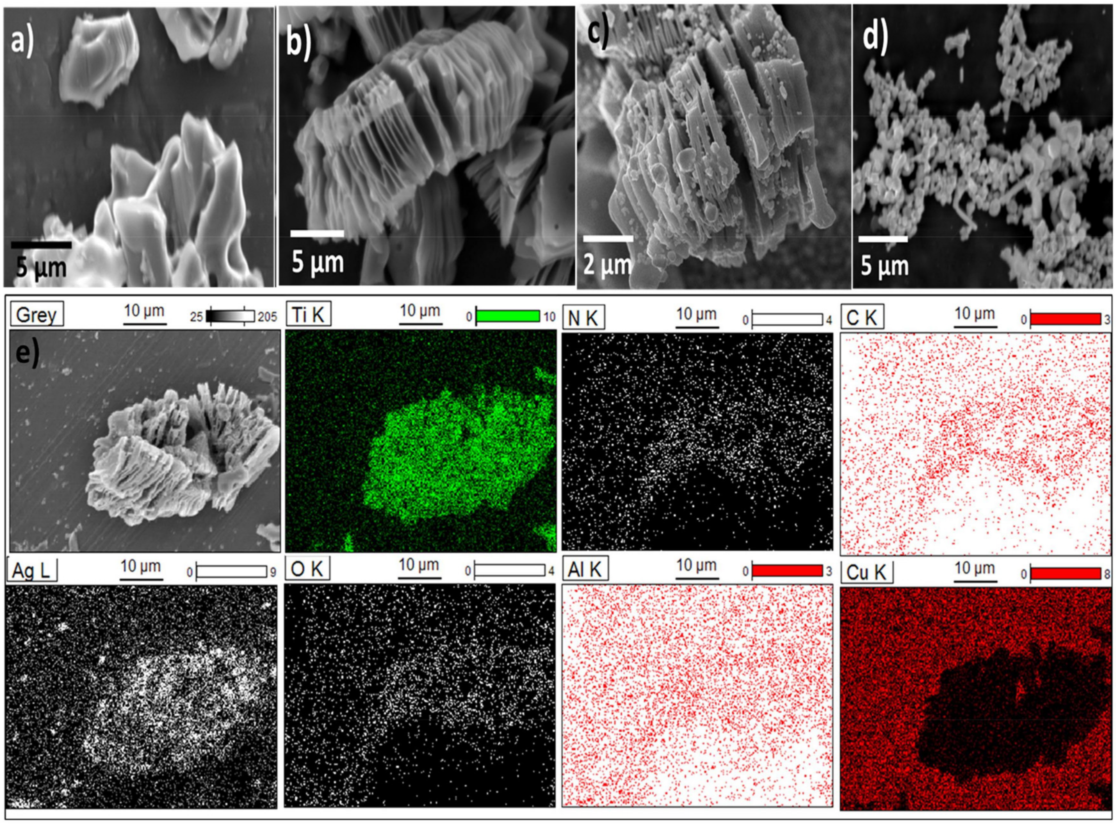

Fig. 2 SEM images of (a) Ti_3AlCN MAX phase, (b) accordion-like multilayered (ML) Ti_3CNT_x MXene, (c) *in situ* grown Ag/Ti_3CNT_x MXene nanocomposites and (d) pure Ag nanoparticles using same microwave-hydrothermal-polyol method and (e) elemental color mapping of Ti, N, C, Ag, O, and Al in Ag/Ti_3CNT_x nanocomposites.

(JCPDS no. 012-0632) (Fig. 3a) vanished utterly, and the shifting of (002) peak from ~9.5° to ~6.2° indicated the formation of Ti_3CNT_x MXene.[25,26,31] Also, an increase in the interlayer *d*-spacing (calculated using Bragg's equation) from 0.93 to 1.42 nm proves the bulk's structural expansion into a multilayer accordion-like structure. This increase in interlayer spacing confirms the formation of layered MXene sheets.[25,31] In the case of the Ag/Ti_3CNT_x, the presence of silver peaks at 38°, 44°, 64°, and 77° as (111), (200), (220) and (311) (JCPDS no: 01-1164) along with the 002 peak of MXene represents the formation of Ag/Ti_3CNT_x.[40,47,48]

We have also measured the water-based colloidal suspension stability as well as the charge at the surface of pure Ag, Ti_3AlCN, ML Ti_3CNT_x, and Ag/Ti_3CNT_x through zeta potential measurement in an aqueous medium at pH 7 (Fig. 3b). Ag/Ti_3CNT_x shows a negative zeta potential of −8.41 ± 0.89 mV, while for Ti_3CNT_x and Ti_3AlCN, it is −2.04 ± 0.56 and −4.67 ± 0.28 mV, respectively.[16,49] Ag/Ti_3CNT_x nanocomposites have better and higher values compared to Ti_3CNT_x, which shows better colloidal stability and more negative charges on its surface. The zeta potential of Ti_3CNT_x is lower than the previously reported Ti_3CNT_x MXene.[26,49] A possible reason could

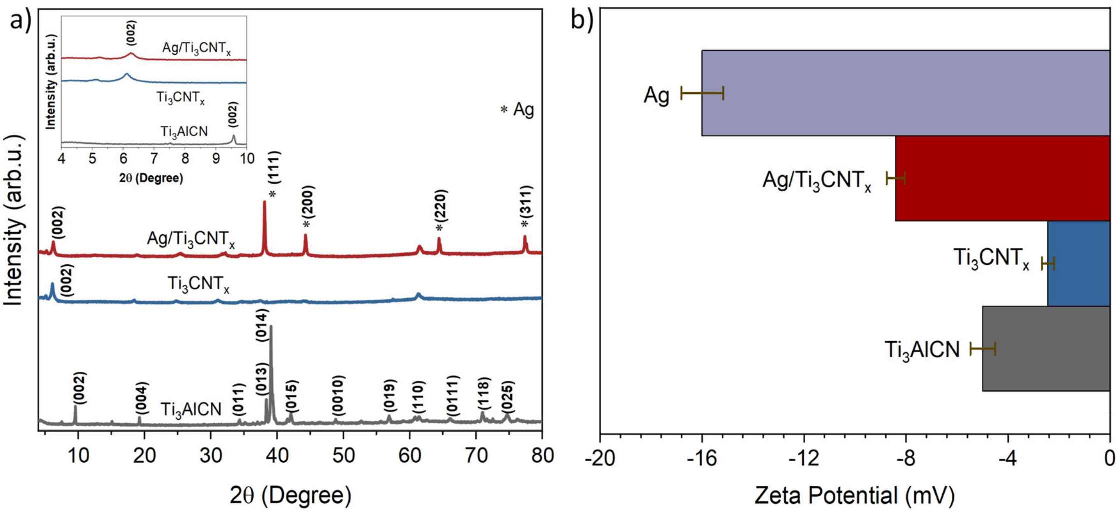

Fig. 3 (a) XRD patterns of the as-synthesized Ti_3AlCN, ML Ti_3CNT_x, and Ag/Ti_3CNT_x nanocomposites and inset shows the enlarged XRD patterns in the range of 4–10° (degree) and (b) zeta-potential of Ti_3AlCN, ML Ti_3CNT_x, Ag/Ti_3CNT_x, and pure Ag in an aqueous medium at pH 7.

be using different etching and synthesis methods compared to conventional methods.[27,29,49] Pure Ag nanoparticle has the highest zeta potential (−16.00 ± 0.82), confirming the better colloidal stability. Further, UV-Vis absorption spectra have also been measured (Fig. S4) in powder form, and silver's characteristic absorption peak is around 300 nm. For Ti_3CNT_x, we have also observed an inflection point around 660 nm, as reported previously.[26]

Based on the results, this microwave-assisted method is suitable for large-scale production of silver nanocomposites with consistent quality and desired silver content. Using silver makes it more affordable than other noble metals, and the process is easy, with added benefits like strong antibacterial and antifungal properties.

3.2. Bactericidal activity

The bactericidal activity of ML Ti_3CNT_x and Ag/Ti_3CNT_x against *E. coli*, *S. aureus*, and *B. subtilis* was evaluated by measuring the optical density (OD) at 610 nm for pristine bacteria and bacteria treated with different concentrations of nanomaterials over a different time interval (0 to 72 h). Performing the antibacterials experiment with nutrients is better because it shows good bacterial growth disorders and helps to determine additional growth parameters. Fig. 4 shows the growth curves of all three bacteria strains with materials (ML Ti_3CNT_x and Ag/Ti_3CNT_x) with concentrations ranging from 0 to 500 mg L^{-1}. It was observed that the inhibition of *E. coli* (Fig. 4a and d) bacteria strain is quite effective compared to *S. aureus* (Fig. 4b and e) and *B. subtilis* (Fig. 4c and f) for Ti_3CNT_x and Ag/Ti_3CNT_x. For example, in the case of *E. coli*, optical density reaches 0.81 ± 0.2 for Ti_3CNT_x and 0.73 ± 0.6 for Ag/Ti_3CNT_x from 0.27 ± 0.2 (control) in 72 hours at 500 mg L^{-1}. While in the case of *S. aureus*, it reaches 0.95 ± 0.3 for Ti_3CNT_x and 0.88 ± 0.4 for Ag/Ti_3CNT_x from 0.32 ± 0.2 (control) in 72 hours at 500 mg L^{-1}. For *B. subtilis*, it reaches 1.24 ± 0.3 for Ti_3CNT_x and 1.00 ± 0.6 for Ag/Ti_3CNT_x from 0.20 ± 0.2 (control) in 72 hours at 500 mg L^{-1}.

Also, the inhibition of bacterial strain growth is dose-dependent, and the bactericidal activity increases with the increase in the concentration of ML Ti_3CNT_x and Ag/Ti_3CNT_x.[9,14] In particular, a 500 mg L^{-1} dose of Ag/Ti_3CNT_x nanocomposites has much more pronounced antibacterial activity than the same concentration of Ti_3CNT_x MXene, especially in the case of the *B. subtilis* bacteria strain. We have also observed (Fig. 4) that each bacterial strain for both materials grew until 24 h, reached its saturation in 48 h, and stopped growing. The current results agree with previously reported data, where hydrophilic $Ti_3C_2T_x$ could effectively attach to bacteria, facilitating their inactivation by direct contact interaction.[9]

For comparison, we have also performed the same experiments for all three bacteria strains (*E. coli*, *S. aureus*, and *B. subtilis*) (Fig. S5) with synthesized pure Ag nanoparticles, which are well-known and standard antibacterial nanomaterials.[40,41,50] At higher concentrations, *i.e.*, 250, 375, and 500 mg L^{-1}, pure Ag shows much better antibacterial activity than ML Ti_3CNT_x and Ag/Ti_3CNT_x. Still, at lower concentrations (such as 16, 32, and 62.5 mg L^{-1}), it shows the same pattern as in the case of Ti_3CNT_x and Ag/Ti_3CNT_x. Therefore, we can conclude that Ti_3CNT_x and Ag/Ti_3CNT_x can be antibacterial.

To better understand and have clear perspectives, we have used eqn (1) to calculate the cell's viability using optical density data at times 0, 8, 16, 24, 48, and 72 h for 125 and 500 mg L^{-1} concentrations of Ti_3CNT_x and Ag/Ti_3CNT_x for all the three-bacteria strains shown in Fig. 5 along with the *p*-value marking for statical significance. It shows that viability is more prominent after 8 h and reduced by 20–40% with $p < 0.05$ (respectively to Ti_3CNT_x and Ag/Ti_3CNT_x) in all three bacterial strains. However, in the case of *S. aureus*, bacterial viability is much more effective and consistent than that of the other two bacteria strains, *E. coli* and *B. subtilis*.

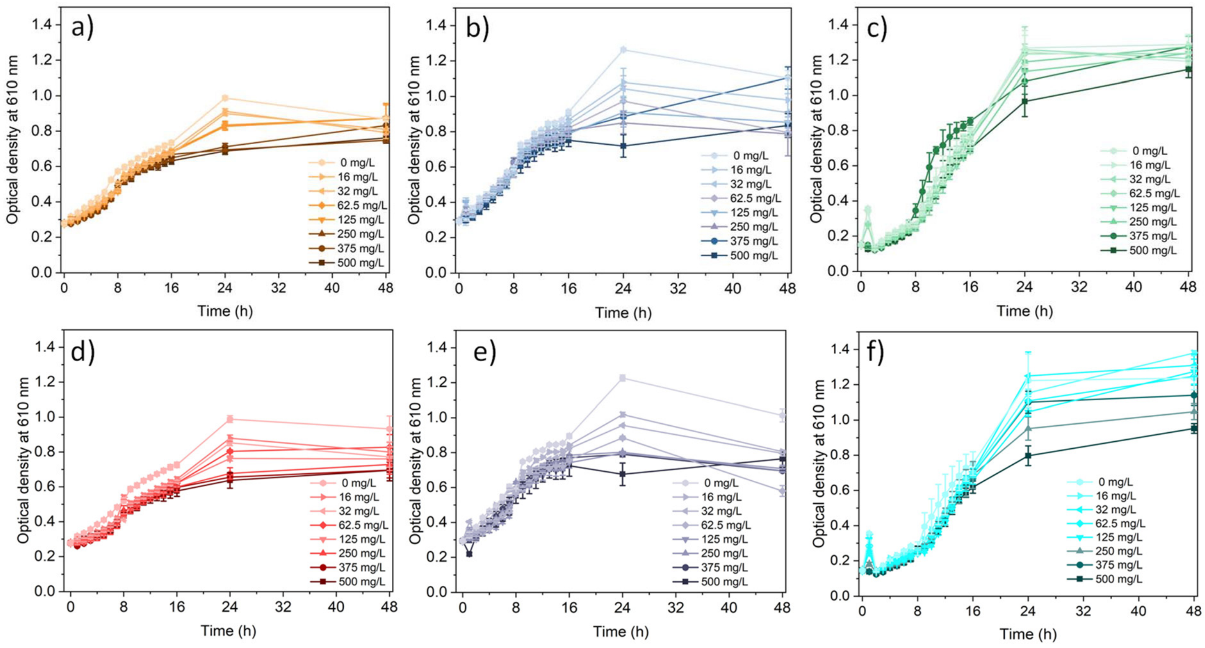

Fig. 4 Optical density growth curves of (a) *E coli*, (b) *S. aureus*, (c) *B. subtilis* after bacteria cells being treated with different concentrations of ML Ti_3CNT_x in Mueller–Hinton broth and (d) *E coli*, (e), *S. aureus* and (f) *B. subtilis* after bacteria cells being treated with different concentrations of Ag/Ti_3CNT_x nanocomposites in Mueller–Hinton broth at 37 °C. Controls were without any materials; pure Mueller–Hinton broth was used (0 mg L^{-1}). Experiments were performed in triplicate, and similar results were obtained from three repeated measurements. Bars display mean ± SD.

It also demonstrates that Ag/Ti_3CNT_x is more effective than Ti_3CNT_x, proving our hypothesis that adding a small amount of Ag into the MXene can enhance its antibacterial properties.[40,51,52] Similar results have also been reported by Ismail *et al.*, who have coated a small amount of Ag on the surface of TiO_2, ZnO, and Fe_2O_3 films on the SLG (soda-lime glass) for antibacterial activity with *Vibrio parahaemolyticus*, *Aeromonas hydrophila*, *and B. subtilis.*[50] They observed higher antibacterial activity of Ag/TiO_2, Ag/ZnO, and Ag/Fe_2O_3 films than pristine ZnO, Fe_2O_3, and TiO_2 films.[50,52,53] Therefore, the *in situ* growth of Ag nanoparticles on ML Ti_3CNT_x MXene surface helps and improves the activity by 15–20% for all three bacteria. The reason for this better antibacterial property could be the surface functionalization of Ti_3CNT_x and the antibacterial properties of Ag nanoparticles. However, it is also believed that the antibacterial activities of MXenes originate from their typical 2D morphology, which enables their sharp edges to penetrate and damage the cell walls of bacteria.[14,54–56]

Further, we have tabulated all the recently reported and relevant MXene and MXene-based nanomaterials in Table S4. This table provides a comprehensive summary of MXene-based nanomaterials, detailing the associated bacterial strains, dosages, and environmental conditions relevant to their biomedical applications. It also highlights the performance of our Ti_3CNT_x and Ag/Ti_3CNT_x composites relative to existing

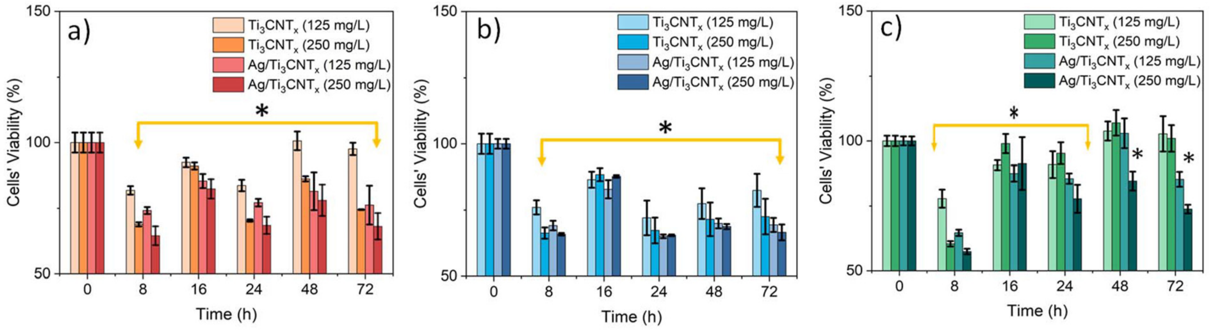

Fig. 5 Cell viability measurements of (a) *E. coli*, (b) *S. aureus*, (c) *B. subtilis* at concentration 125 and 250 mg L^{-1} of ML Ti_3CNT_x and Ag/Ti_3CNT_x. Experiments were performed in triplicate, and similar results were obtained from three repeated measurements. Bars display mean ± SD. All tests were carried out in triplicate (mean ± SD; $n = 3$; $*p < 0.05$). p-values were calculated with the Student's test.

materials and provides a broad overview of MXene's current use in biomedical applications.

3.3 Mechanism of nanocomposites interaction with *E. coli*, *S. aureus*, and *B. subtilis*

Further, to understand the antibacterial mechanism and interaction between bacteria and nanomaterials, SEM images were captured. The morphological changes of bacterial cells induced by Ti_3CNT_x and Ag/Ti_3CNT_x were observed through SEM images (Fig. 6), providing deeper insight into their antibacterial process. As shown in the SEM images, most *E. coli* (Fig. 6a and d) and *B. subtilis* (Fig. 6b and e) cells suffered from significant membrane damage with cell hydrolysis. Cell shrinking and flattening were also observed, indicating the loss of viability and damage to the cell membrane.

All three bacterial strains suffered from the prevalent membrane damage and cytoplasm leakage, while some still maintained the membrane integrity (Fig. 6d–f), but were deformed. Also, MXene, being hydrophilic, may increase the bacteria's contact with the membrane surface, resulting in the rupture of the cell membrane and inactivation of bacteria according to the direct contact-killing mechanism.[10,14,15,29] According to existing literature, the antibacterial mechanism of MXenes often involves direct interaction with bacterial membranes. This includes electrostatic binding between the negatively charged MXene surfaces and the phospholipid components of the cell membrane, leading to membrane disruption, MXene accumulation, and ultimately cell death.[9,19] The negative zeta potentials observed for our nanocomposites (Ag/Ti_3CNT_x −8.41 mV, while for Ti_3CNT_x −2.04, respectively) support the possibility of such interactions. However, this proposed mechanism requires further experimental validation.

The presence of Ag with ML MXene contributes to bactericidal activity. The Ag nanoparticles could interact with bacterial cell membranes, either engulfed by the bacteria or through adhering to the surface. Similar observations were noticed and reported for graphene, GO, and CNTs, where the bacteria's cell membrane was disrupted, and the leakage of their cytoplasmic content after direct contact with graphene-based material.[8,53,54,57–59]

Recent studies suggest that the antibacterial activity and cytotoxicity of MXenes (mostly $Ti_3C_2T_x$) are governed by multiple factors, including particle size, surface charge, oxidation state, exposure duration, and the specific etching or delamination methods employed during synthesis.[60–62] The underlying mechanisms often involve direct interactions with cellular membranes, where electrostatic binding between negatively charged MXene surfaces and membrane phospholipids leads to membrane disruption, MXene accumulation, and ultimately cell death.[14,19,61] This study serves as a foundational step, paving the way for future biomedical research focused on carbonitride-based MXenes.

3.4 Antibacterials studies of actual samples for food packaging applications

Antimicrobial efficiency is crucial in food packaging for controlling microorganisms that cause food-borne illnesses. Bare plastic or paper packaging lacks antimicrobial activity.[1–3,12] To understand the real-world application of synthesized nanocomposites based on their bactericidal and microbial activity, we tested them on actual samples such as tissue paper, bread, and cheese using bacteria like *E. coli*, *B. subtilis*, and *S. aureus*.

Fig. 7 shows a digital photograph of tissue paper at 37 °C with all three bacteria and synthesized nanomaterials (Ag, Ti_3CNT_x, and Ag/Ti_3CNT_x) compared to a blank sample. No visible changes were observed in the tissue paper except on the 8th day with *E. coli* and *S. aureus*, where the tissue paper color faded. At room temperature (Fig. S6), no visible changes were

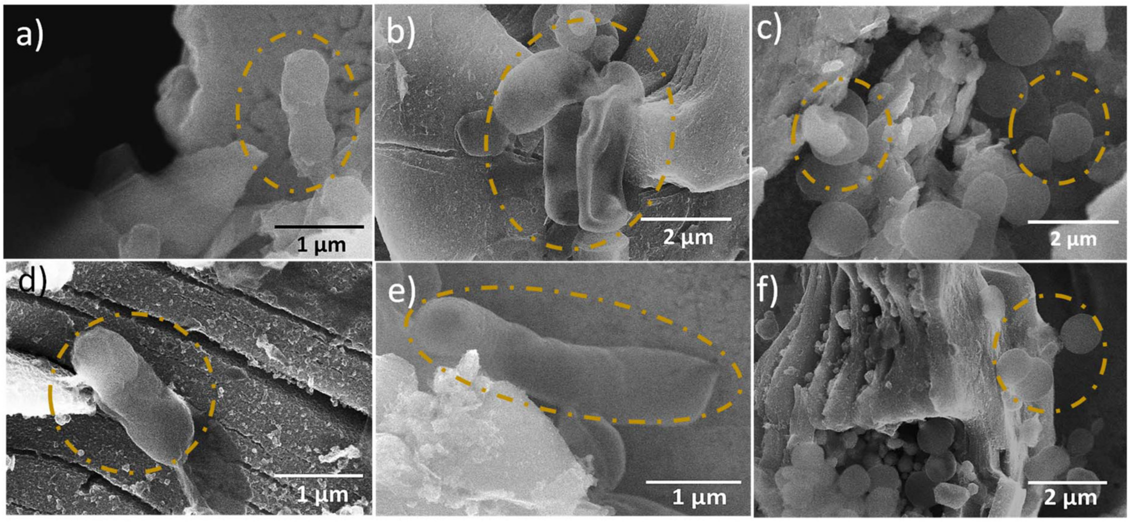

Fig. 6 SEM images of bacteria adsorption on the surface of ML Ti_3CNT_x (a) *E. coli*, (b) *B. subtilis*, (c) *S. aureus* and Ag/Ti_3CNT_x (d) *E. coli*, (e) *B. subtilis*, (f) *S. aureus*. The enclosed orange circle highlights the respective bacteria.

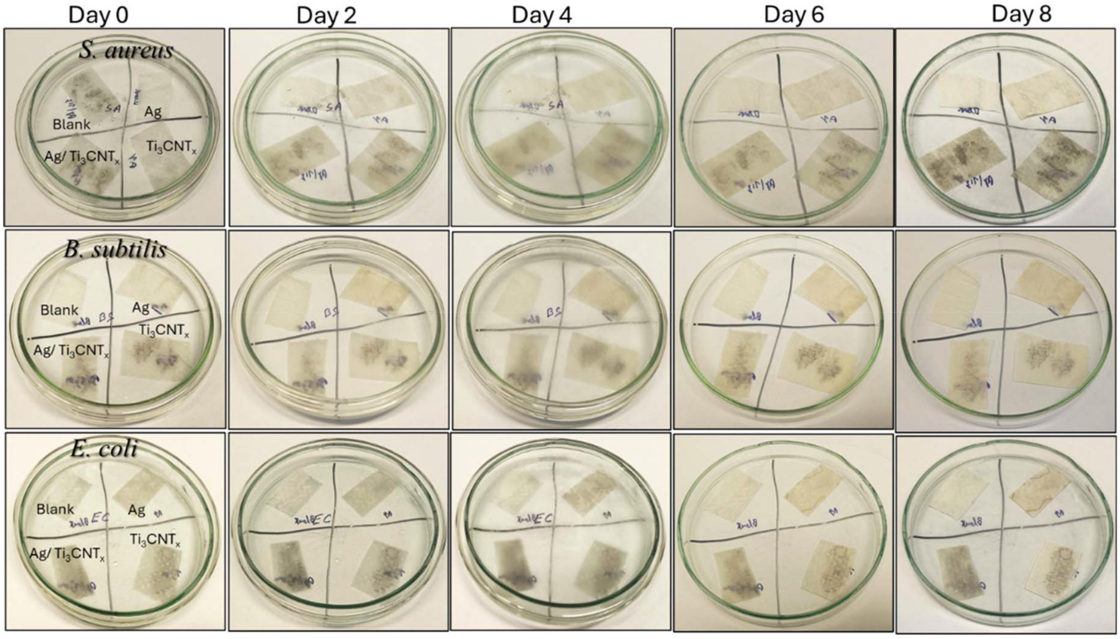

Fig. 7 Digital photographs of tissue paper at 37 °C for three bacteria strains, *E. coli*, *B. subtilis*, and *S. aureus*, for blank, Ag, ML Ti$_3$CNT$_x$, and Ag/Ti$_3$CNT$_x$ from day 0 to day 8 with 1-day intervals.

seen until the 8th day. Under an optical microscope, each bacterial strain was visible in both conditions (Fig. S7–S10). However, bacterial growth gradually reduced from the blank to the Ag/Ti$_3$CNT$_x$ nanocomposites (Fig. S7 and S8). The bacteria's growth followed the same trend at room temperature but was less pronounced (Fig. S9 and S10). These results match the previous reports where MXene with other polymers or as a thin film has shown relatively better results.[3,57]

In the case of bread samples, the bread began degrading from day 4, and by day 8 at 37 °C (Fig. S11). It was completely damaged and black, likely due to mold (*Rhizopus stolonifer*) growth. It is well reported that white bread tends to mold more quickly because it's baked with yeast.[63,64] *E. coli* showed faster bacterial growth, which was slower in *B. subtilis* and *S. aureus*. At room temperature (Fig. S12), degradation was slower for all bacterial strains. We also captured images of bacterial solutions at 37 °C and room temperature at two magnifications (10 and 50 μm) for a clear understanding. Pure silver showed better results than ML Ti$_3$CNT$_x$, and Ag/Ti$_3$CNT$_x$, with similar trends observed for their bactericidal activities. Ag/Ti$_3$CNT$_x$ showed improved results compared to Ti$_3$CNT$_x$ (Fig. S13–S16).

Furthermore, we have also tested cheese, which is shown in Fig. S17 and S18. Here, we have also observed the same trend as with bread. At 37 °C, the cheese gets damaged by the 8th day, especially for *E. coli.* However, in the case of the other two, not much visual change can be seen. A similar trend could be observed in the case of a room-temperature batch. However, we can see the growth of bacteria when the images were captured by preparing a bacterial solution. Fig. S20 shows that *B. subtilis* has higher growth than the other two bacteria. However, the reduction of bacteria is observed with an order Ag, Ag/Ti$_3$CNT$_x$ followed by Ti$_3$CNT$_x$ (Fig. S19–S22). We can also observe small and random amounts of multilayer MXene in these images. Few reports have been published where MXene has been successfully used for food preservation, and it can increase the shelf life of the food. Although primarily intended for industrial applications, further tests are needed, including stability assessments under different storage conditions, migration analyses to ensure food safety, sensory evaluations, and toxicological testing.[3,12,32]

Ultimately, these MXene-based nanocomposites are suitable for food packaging applications. However, further cytotoxicity and detailed experiments are necessary for better understanding and industrial use. Also, careful market research and safety checks are needed before these materials can be sold commercially. Additionally, to fully comprehend the antibacterial effects, several factors need exploration, including the impact of different Ag morphologies, particle size, when combined with MXene, the influence of MXene surface functional groups, the impact of flake size, surface charge, oxidation state, exposure duration, and the specific etching or delamination methods. These investigations will aid in developing MXene-based antimicrobial coatings for wound dressings, food packaging industries, and water purification membranes.[3,12,32,51,57]

4 Conclusions

Our study has successfully demonstrated the efficacy of the microwave-assisted hydrothermal method in synthesizing MXene-based nanocomposites. This innovative approach offers advantages over traditional wet chemical etching methods, including faster processing times, higher-quality products, and precise control over the final product's size, shape, and crystallinity. The microwave-assisted hydrothermal method also effectively prevents oxidation, ensuring the stability and uniformity of the synthesized nanocomposites.

For the first time, we have thoroughly investigated the antibacterial properties of Ti_3CNT_x MXene and Ag/Ti_3CNT_x MXene nanocomposites and real-world applications in the food packaging industry. Our findings reveal that these nanocomposites exhibit superior antibacterial activity compared to pristine MXene. Specifically, the surface decoration of Ti_3CNT_x with silver nanoparticles significantly enhances the antibacterial efficacy of the resulting composite against a range of bacterial strains, including Gram-negative *E. coli* and Gram-positive *S. aureus* and *B. subtilis*. The enhanced antibacterial properties can be attributed to the synergistic effects of MXene's rich active sites and the well-known antimicrobial activity of silver nanoparticles.

The findings reveal that pristine ML Ti_3CNT_x exhibits antibacterial properties similar to $Ti_3C_2T_x$ MXene. However, Ag/Ti_3CNT_x demonstrates significantly better antibacterial activity (15–20% higher) than pristine ML Ti_3CNT_x MXene alone. This discovery opens the door for further extensive studies on various carbonitride-based MXene materials and MXene-based nanocomposites.

Our results demonstrate the potential of Ti_3CNT_x MXene-based nanocomposites as effective antimicrobial agents for various applications, including biomedical devices, antimicrobial coatings, wound healing, food packaging, and water purification systems. The ability to control the synthesis process and produce uniform, high-quality nanocomposites opens new avenues for their use in diverse fields.

We encourage researchers to explore new synthesis methods and their impact on the functional properties of advanced materials. The microwave-assisted hydrothermal method streamlines the synthesis process and enhances the resulting nanocomposites' performance characteristics. This approach could be extended to other MXene-based materials and nanocomposites, potentially leading to new advancements in their processing and applications.

Author contributions

MC designed the concept and content of the experiment, prepared and characterized samples, collected and analyzed the obtained results, prepared the actual sample measurements and analysis, prepared the original manuscript, MJ designed the antibacterials studies and further helped in performing and analyzing the results, MAKP performed the FT-IR and UV-Vis measurements, AG and WB helped and performed the synthesis of material, FT-IR and zeta potential measurements, DM carried out XRD measurements, AT and MN synthesized the MAX phase (Ti_3AlCN) and corrected the original manuscript, AJ acquired funds, coordinated and supervised the preparation of the manuscript, coordinated the research, and corrected the original manuscript. The manuscript was written with contributions from all authors. All authors have approved the final version of the manuscript.

Conflicts of interest

There are no conflicts to declare.

Data availability

The data supporting this article have been included in the SI. The supporting information includes EDS, FT-IR, and UV-Vis spectra of the synthesized materials, along with optical density growth curves of Ag nanoparticles. Additionally, both digital and optical images of all real samples and bacteria are provided. See DOI: **https://doi.org/10.1039/d5nr02098k**.

Also, the data that support the findings of this manuscript are available upon request from the corresponding author.

Acknowledgements

This work was funded by National Science Centre (NCN) within the framework of the research project 'OPUS-18' (UMO-2019/35/B/ST5/02538). The Warsaw University of Technology funded the research within the Excellence Initiative: Research University (IDUB) program (POST-DOC II program). MC acknowledges the financial support from the research project MINIATURA 8 (UMO-2024/08/X/ST5/01177). MJ acknowledges the financial support from the research project 'OPUS-18' (UMO-2019/35/B/ST5/02538) and 'PRELUDIUM-22' (UMO-2023/49/N/ST11/03574), the Foundation for Polish Science (FNP, Scholarship START program), and the ID-UB project (Scholarship Plus program). MAKP acknowledges the financial support from the research project "PRELUDIUM-21" (UMO-2022/45/N/ST5/02472).

References

1 Q. Chaudhry, M. Scotter, J. Blackburn, B. Ross, A. Boxall, L. Castle, R. Aitken and R. Watkins, *Food Addit. Contam.*, 2008, **25**(3), 241–258.
2 T. V. Duncan, *J. Colloid Interface Sci.*, 2011, **363**, 1–24.
3 W. Liu, S. Kang, Q. Zhang, S. Chen, Q. Yang and B. Yan, *Food Chem.*, 2023, **410**, 135405.
4 C. V. Garcia, G. H. Shin and J. T. Kim, *Trends Food Sci. Technol.*, 2018, **82**, 21–31.
5 T. M. Uddin, A. J. Chakraborty, A. Khusro, B. R. M. Zidan, S. Mitra, T. B. Emran, K. Dhama, M. K. H. Ripon, M. Gajdács, M. U. K. Sahibzada, M. J. Hossain and N. Koirala, *J. Infect. Public Health*, 2021, **14**, 1750–1766.
6 D. R. Dodds, *Biochem. Pharmacol.*, 2017, **134**, 139–146.

7 J. L. Fortman and A. Mukhopadhyay, *Trends Microbiol.*, 2016, **24**, 515–517.

8 E. Alp, F. Olivieri, M. Aulitto, R. Castaldo, P. Contursi, M. Cocca and G. Gentile, *Surf. Interfaces*, 2024, **55**, 105307.

9 K. Rasool, K. A. Mahmoud, D. J. Johnson, M. Helal, G. R. Berdiyorov and Y. Gogotsi, *Sci. Rep.*, 2017, **7**, 1598.

10 K. Salimiyan rizi, *J. Mol. Struct.*, 2022, **1262**, 132958.

11 F. Seidi, A. Arabi Shamsabadi, M. Dadashi Firouzjaei, M. Elliott, M. R. Saeb, Y. Huang, C. Li, H. Xiao and B. Anasori, *Small*, 2023, **19**(14), 2206716.

12 X. Zhou, Y. Hao, Y. Li, J. Peng, G. Wang, W.-J. Ong and N. Li, *Nano Sel.*, 2022, **3**, 1123–1147.

13 Y. Gao, Y. Dong, S. Yang, A. Mo, X. Zeng, Q. Chen and Q. Peng, *J. Colloid Interface Sci.*, 2022, **617**, 533–541.

14 K. Rasool, M. Helal, A. Ali, C. E. Ren, Y. Gogotsi and K. A. Mahmoud, *ACS Nano*, 2016, **10**, 3674–3684.

15 M. Sadey Salmi, U. Ahmed, N. Aslfattahi, S. Rahman, J. George Hardy and A. Anwar, *RSC Adv.*, 2022, **12**, 33142–33155.

16 A. Rozmysłowska-Wojciechowska, T. Wojciechowski, W. Ziemkowska, L. Chlubny, A. Olszyna and A. M. Jastrzębska, *Appl. Surf. Sci.*, 2019, **473**, 409–418.

17 A. M. Jastrzębska, A. Szuplewska, T. Wojciechowski, M. Chudy, W. Ziemkowska, L. Chlubny, A. Rozmysłowska and A. Olszyna, *J. Hazard. Mater.*, 2017, **339**, 1–8.

18 A. Rozmysłowska-Wojciechowska, E. Karwowska, S. Poźniak, T. Wojciechowski, L. Chlubny, A. Olszyna, W. Ziemkowska and A. M. Jastrzębska, *RSC Adv.*, 2019, **9**, 4092–4105.

19 A. Wojciechowska, M. Jakubczak, D. Moszczyńska, A. Wójcik, K. Prenger, M. Naguib and A. M. Jastrzębska, *Biomater. Adv.*, 2023, **153**, 213581.

20 K. R. G. Lim, M. Shekhirev, B. C. Wyatt, B. Anasori, Y. Gogotsi and Z. W. Seh, *Nat. Synth.*, 2022, **1**, 601–614.

21 B. Anasori, M. Naguib and Guest Editors, *MRS Bull.*, 2023, **48**, 238–244.

22 M. Naguib, O. Mashtalir, J. Carle, V. Presser, J. Lu, L. Hultman, Y. Gogotsi and M. W. Barsoum, *ACS Nano*, 2012, **6**, 1322–1331.

23 M. Naguib, R. A. Adams, Y. Zhao, D. Zemlyanov, A. Varma, J. Nanda and V. G. Pol, *Chem. Commun.*, 2017, **53**, 6883–6886.

24 Y. Xu, F. Wang, S. Lei, Y. Wei, D. Zhao, Y. Gao, X. Ma, S. Li, S. Chang, M. Wang and H. Jing, *Chem. Eng. J.*, 2023, **452**, 139392.

25 I. Ashraf, S. Ahmad, D. Dastan and M. Iqbal, *J. Alloys Compd.*, 2023, **952**, 170043.

26 M. A. K. Purbayanto, D. Bury, M. Chandel, Z. D. Shahrak, V. N. Mochalin, A. Wójcik, D. Moszczyńska, A. Wojciechowska, A. Tabassum, M. Naguib and A. M. Jastrzębska, *ACS Appl. Mater. Interfaces*, 2023, **15**, 44075–44086.

27 J. Zhu, M. Wang, M. Lyu, Y. Jiao, A. Du, B. Luo, I. Gentle and L. Wang, *ACS Appl. Nano Mater.*, 2018, **1**, 6854–6863.

28 A. Iqbal, F. Shahzad, K. Hantanasirisakul, M.-K. Kim, J. Kwon, J. Hong, H. Kim, D. Kim, Y. Gogotsi and C. M. Koo, *Science*, 2020, **369**, 446–450.

29 K. Liang, A. Tabassum, M. Kothakonda, X. Zhang, R. Zhang, B. Kenney, B. D. Koplitz, J. Sun and M. Naguib, *Mater. Rep.: Energy*, 2022, **2**, 100075.

30 M. Naguib, W. Tang, K. L. Browning, G. M. Veith, V. Maliekkal, M. Neurock and A. Villa, *ChemCatChem*, 2020, **12**, 5733–5742.

31 Z. Zhao, X. Qian, H. Zhu, Y. Miao and H. Ye, *ChemistrySelect*, 2022, **7**, e202104176.

32 A. M. Amani, A. Rahbar, E. Vafa, L. Tayebi, M. Abbasi, H. Kamyab, S. Chelliapan, S. R. Kasaee, A. Vaez and S. Mosleh-Shirazi, *Mater. Today Commun.*, 2024, **41**, 110774.

33 R. P. Pandey, K. Rasool, V. E. Madhavan, B. Aïssa, Y. Gogotsi and K. A. Mahmoud, *J. Mater. Chem. A*, 2018, **6**, 3522–3533.

34 X. Zhu, Y. Zhu, K. Jia, B. Sielu Abraha, Y. Li, W. Peng, F. Zhang, X. Fan and L. Zhang, *Nanoscale*, 2020, **12**, 19129–19141.

35 X. Hou, H. Wang, X. Yao, Q. Zhou and X. Niu, *ACS Nano*, 2025, **19**, 17709–17727.

36 X. Liu, H. Xie, S. Zhuo, Y. Zhou, M. S. Selim, X. Chen and Z. Hao, *Nanomaterials*, 2023, **13**, 958.

37 S. Wen, Y. Xiong, S. Cai, H. Li, X. Zhang, Q. Sun and R. Yang, *Nanoscale*, 2022, **14**, 16572–16580.

38 T. Jílková, E. Miliutina, A. Trelin, Z. Kolská, V. Švorčík, O. Lyutakov and R. Elashnikov, *Mater. Adv.*, 2025, **6**, 4795–4803.

39 P. Singh, M. Halder, S. Ray, A. Bose and K. Sen, *Mater. Adv.*, 2020, **1**, 2937–2952.

40 Q. Liu, Y. Zhang, Y. Liu, Z. Liu, B. Zhang and Q. Zhang, *J. Alloys Compd.*, 2021, **860**, 158151.

41 S. Silver, L. T. Phung and G. Silver, *J. Ind. Microbiol. Biotechnol.*, 2006, **33**, 627–634.

42 B. Khodashenas and H. R. Ghorbani, *Arabian J. Chem.*, 2019, **12**, 1823–1838.

43 S. Głowniak, B. Szczęśniak, J. Choma and M. Jaroniec, *Adv. Mater.*, 2021, **33**, 2103477.

44 L.-Y. Meng, B. Wang, M.-G. Ma and K.-L. Lin, *Mater. Today Chem.*, 2016, **1–2**, 63–83.

45 N. Devi, S. Sahoo, R. Kumar and R. K. Singh, *Nanoscale*, 2021, **13**, 11679–11711.

46 T. Zhao, R. Sun, S. Yu, Z. Zhang, L. Zhou, H. Huang and R. Du, *Colloids Surf., A*, 2010, **366**, 197–202.

47 J. Meng, J. Luo, H. Wang, Y. Quan, J. Li and X. Sun, *Chem. Commun.*, 2022, **58**, 6821–6824.

48 H. Zhou, N. K. L. Jiresse, W. Zhang, Z. Chen, Y. Zhang and J. Zhang, *J. Mater. Res.*, 2021, **36**, 5002–5012.

49 M. Naguib, R. R. Unocic, B. L. Armstrong and J. Nanda, *Dalton Trans.*, 2015, **44**, 9353–9358.

50 A. A. Ismail, L. Al-Hajji, I. S. Azad, A. Al-Yaqoot, N. Habibi, M. Alseidi and S. Ahmed, *J. Taiwan Inst. Chem. Eng.*, 2023, **142**, 104627.

51 M. Jakubczak, E. Karwowska, A. Rozmysłowska-Wojciechowska, M. Petrus, J. Woźniak, J. Mitrzak and A. M. Jastrzębska, *Materials*, 2021, **14**, 182.

52 M. Jakubczak, D. Bury, A. Wojciechowska, E. Karwowska and A. M. Jastrzębska, *Mater. Chem. Phys.*, 2023, **297**, 127333.

53 M. Jakubczak, E. Karwowska, A. Fiedorczuk and A. M. Jastrzębska, *RSC Adv.*, 2021, **11**, 18509–18518.

54 S. Liu, T. H. Zeng, M. Hofmann, E. Burcombe, J. Wei, R. Jiang, J. Kong and Y. Chen, *ACS Nano*, 2011, **5**, 6971–6980.

55 A. Szuplewska, D. Kulpińska, M. Jakubczak, A. Dybko, M. Chudy, A. Olszyna, Z. Brzózka and A. M. Jastrzębska, *Adv. Drug Delivery Rev.*, 2022, **182**, 114099.

56 M. A. K. Purbayanto, M. Jakubczak, D. Bury, V. G. Nair, M. Birowska, D. Moszczyńska and A. Jastrzębska, *ACS Appl. Nano Mater.*, 2022, **5**, 5373–5386.

57 M. Dong, E. Bilotti, H. Zhang and D. G. Papageorgiou, *Int. J. Biol. Macromol.*, 2024, **265**, 130520.

58 S. Kang, M. Pinault, L. D. Pfefferle and M. Elimelech, *Langmuir*, 2007, **23**, 8670–8673.

59 J. Li, G. Wang, H. Zhu, M. Zhang, X. Zheng, Z. Di, X. Liu and X. Wang, *Sci. Rep.*, 2014, **4**, 4359.

60 S. Sagadevan and W.-C. Oh, *J. Drug Delivery Sci. Technol.*, 2023, **85**, 104569.

61 S. N. Sankar, G. Araujo, J. Fernandes, F. Cerqueira, P. Alpuim, A. R. Ribeiro, F. Lebre, E. Alfaro-Moreno, E. Placidi, S. Marras and A. Capasso, *Adv. Mater. Interfaces*, 2024, **11**, 2400203.

62 G. P. Lim, C. F. Soon, N. L. Ma, M. Morsin, N. Nayan, M. K. Ahmad and K. S. Tee, *Environ. Res.*, 2021, **201**, 111592.

63 A. Liu, R. Xu, S. Zhang, Y. Wang, B. Hu, X. Ao, Q. Li, J. Li, K. Hu, Y. Yang and S. Liu, *Front. Microbiol.*, 2022, **13**, 924398.

64 A. Peter, L. Mihaly-Cozmuta, A. Mihaly-Cozmuta, C. Nicula, W. Ziemkowska, D. Basiak, V. Danciu, A. Vulpoi, L. Baia, A. Falup, G. Craciun, A. Ciric, M. Begea, C. Kiss and D. Vatuiu, *Food Chem.*, 2016, **197**, 790–798.